9/21/20
SAND2020-10060C

1

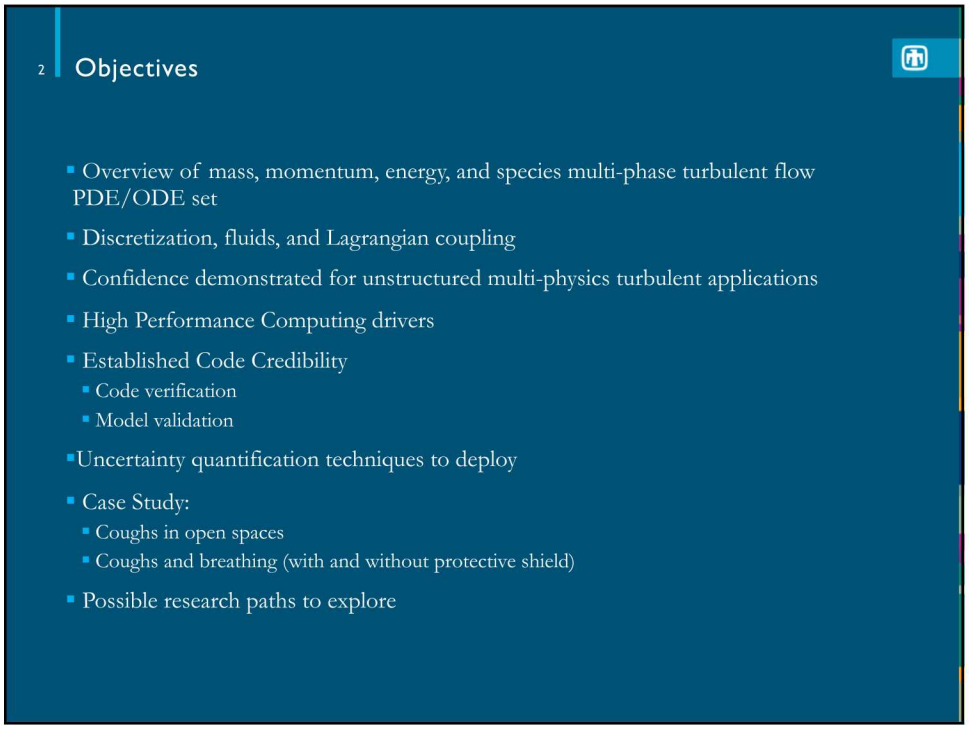

2

3 Proposed Math Model Suite (Eulerian)

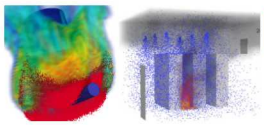

- Variable-density low-Mach Eulerian/point-Lagrangian multi-physics coupling
- Large-eddy simulation-based (low-pass spatial filter); RANS supported, not considered
- S_k represents coupling from Lagrangian evolution and represents source/sink of mass, momentum, energy, and species

$$\int \frac{\partial \bar{\rho}}{\partial t} \mathrm{d}V + \int \bar{\rho} \tilde{u}_j n_j \mathrm{d}S = \int S_m \mathrm{d}V,$$

$$\int \frac{\partial \bar{\rho} \tilde{u}_i}{\partial t} \mathrm{d}V + \int \bar{\rho} \tilde{u}_i \tilde{u}_j n_j \mathrm{d}S = \int \tilde{\sigma}_{ij} n_j \mathrm{d}S - \int \tau_{ij}^{sgs} n_j \mathrm{d}S + \int (\bar{\rho} - \rho_\circ) g_i \mathrm{d}V + \int S_{u_i} \mathrm{d}V \qquad \sigma_{ij} = 2\mu \tilde{S}_{ij}^* - \bar{P}\delta_{ij}, \quad \tilde{S}_{ij}^* = \tilde{S}_{ij} - \frac{1}{3}\delta_{ij}\tilde{S}_{kk}$$

$$\int \frac{\partial \bar{\rho} \tilde{\phi}}{\partial t} \mathrm{d}V + \int \bar{\rho} \tilde{\phi} \tilde{u}_j n_j \mathrm{d}S = -\int \bar{q}_j n_j \mathrm{d}S - \int \tau_{\phi,j}^{sgs} n_j \mathrm{d}S + \int S_\phi \mathrm{d}V.$$

$$\bar{q}_j = -\overline{\left[\frac{\mu}{\mathrm{Pr}}\frac{\partial h}{\partial x_j} - \frac{\mu}{\mathrm{Pr}}\sum_{k=1}^{K} h_k \frac{\partial Y_k}{\partial x_j}\right]} - \frac{\mu}{\mathrm{Sc}}\sum_{k=1}^{K} h_k \frac{\partial Y_k}{\partial x_j}. \qquad \mathrm{Le} = \frac{\mathrm{Sc}}{\mathrm{Pr}} = \frac{\alpha}{D}. \qquad \bar{q}_j = -\frac{\mu}{\sigma}\frac{\partial \tilde{\phi}}{\partial x_i},$$

$$\tau_{ij}^{sgs} \equiv \bar{\rho}(\widetilde{u_i u_j} - \tilde{u}_i \tilde{u}_j). \qquad \tau_{h,j}^{sgs} \equiv \bar{\rho}\left(\widetilde{\phi u_j} - \tilde{\phi}\tilde{u}_j\right). \qquad \tau_{ij}^{sgs} - \frac{\tau_{kk}^{sgs}}{3}\delta_{ij} = -2\mu^{sgs}\tilde{S}_{ij}^*.$$

Multiple LES models supported…

3

4 Proposed Math Model Suite (point-Lagrangian)

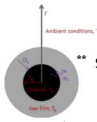

** Stefan flow

- Spherical Lagrangian droplets

Relaxation time $\tau_p = \dfrac{4\rho_p d_p}{3\rho_g C_D |\mathbf{u}_g - \mathbf{u}_p|}.$

$$\frac{dx_{p,i}}{dt} = u_{p,i}.$$

Particle Reynolds number $Re_p = \dfrac{\rho_g d_p |\mathbf{u}_g - \mathbf{u}_p|}{\mu_g}$

Circa 1950s (Spalding, 1953)

Subgrid fluctuations

$$C_D = 24(1 + Re_p)^{2/3}/Re_p \text{ for } Re_p < 1000.$$

$$\frac{du_{p,i}}{dt} = \frac{(u_{g,i} - u_{p,i})}{\tau_p} + \left(\frac{\rho_p - \rho_g}{\rho_p}\right) g_i,$$

Drag coefficient; $C_D = 24/Re_p$ provides limiting settling velocity, u_p

$$C_D = 0.424 \text{ for } Re_p > 1000$$

$$u_p = \frac{d_p^2 (\rho_p - \rho_f) g}{18\mu_p} \qquad B_T = (1 + B_M)^{\frac{Pr}{Sc}\frac{\hat{S}c}{\hat{N}u}} - 1.$$

$$c_p m_p \frac{dT_p}{dt} = \dot{m}\left(\frac{h_f - h_{f,p}}{B_T} - h_v\right),$$

Spalding heat and mass transfer number

$$B_M = \frac{Y_f - Y_g}{Y_p - Y_f}.$$

$$\frac{dm_p}{dt} = -\dot{m}.$$

Raoult's law and Clausius/Clapeyron (liquid/vapor equilibrium)

$$\hat{N}u = \frac{Nu}{Nu_0} = \left(1 + 0.3Pr^{\frac{1}{2}}Re_p^{\frac{1}{2}}\right),$$

Ranz-Marshall correlation (1952)

$$\dot{m} = 4\pi r_p \frac{\mu}{Sc}\hat{Sh}\ln(1 + B_T), \qquad \hat{Sh} = \frac{Sh}{Sh_0}\left(1 + 0.3Sc^{\frac{1}{2}}Re_p^{\frac{1}{2}}\right).$$

See Fuego manual, or excellent derivation under Wikipedia: https://en.wikipedia.org/wiki/Droplet_vaporization **

4

5 Chosen Discretization:
Control-Volume Finite Element Method (CVFEM)

- A combination between the edge-based vertex-centered and FEM is the method known as Control Volume Finite Element (CVFEM) (Hex, Tet, Pyr, Wedge)
- A dual mesh is constructed to obtain flux and volume quadrature locations
- As with FEM, a basis is defined:

$$T(x_k) \approx \sum_{i=1}^{npe} N_i(x_k) T_i \qquad \frac{\partial T(x_k)}{\partial x_j} \approx \sum_{i=1}^{npe} \frac{\partial N_i(x_k)}{\partial x_j} T_i$$

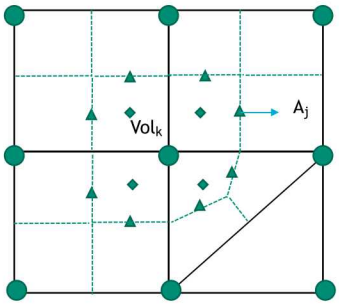

dual-volume definition

- Edge-based assembles A_j and Vol_k to edges and nodes, respectively

- Integration-by-parts over test function w:

$$\int w\rho C_p \frac{\partial T}{\partial t} dV + \int \frac{\partial w}{\partial x_j} \lambda \frac{\partial T}{\partial x_j} dV - \int w\, \lambda \frac{\partial T}{\partial x_j} n_j dS = 0$$

- However, define a test function, w, as a piece-wise constant function (Heaviside) to be 1 inside the dual volume and 0 outside. Gradient is a Dirac-delta function: $\frac{\partial w}{\partial x_j} = -n_j \delta(x_j - x^{IP}{}_j)$
- Leading to: $\int \rho C_p \frac{\partial T}{\partial t} dV - \int \lambda \frac{\partial T}{\partial x_j} n_j\, dS = 0$

5

6 Control-Volume Finite Element Method Attributes

- CVFEM can be viewed as Petrov-Galerkin method
- The method can also be promoted in polynomial space, see Domino, *CTRSP*, 2014 as a first example of low-Mach fluids algorithm – or Domino, *JCP*, 2018
- Research Thrust: Possible higher efficiency on NGP due to increased local work)
- However, suitability of higher-order for LES is an open argument – especially when other errors/uncertainties exist

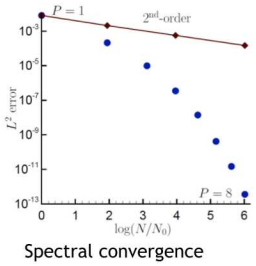

Spectral convergence

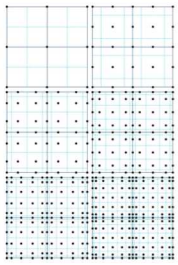

Dual-volume for promoted quad4

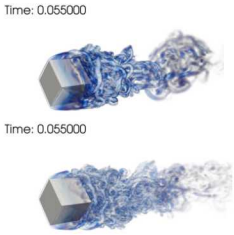

Rotating cube (Re 4000, RPM 3600)
P=1 (top) and P=2 (bottom)

6

7 Control-Volume Finite Element Method Attributes

- CVFEM can be viewed as Petrov-Galerkin method
- The method can also be promoted in polynomial space, see Domino, *CTRSP*, 2014 as a first example of low-Mach fluids algorithm – or Domino, *JCP*, 2018
- Research Thrust: Possible higher efficiency on NGP due to increased local work)
- However, suitability of higher-order for LES is an open argument – especially when other errors/uncertainties exist

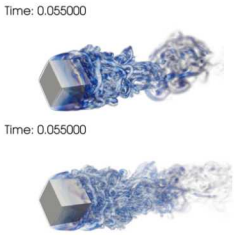

Rotating cube (Re 4000, RPM 3600)
P=1 (top) and P=2 (bottom)

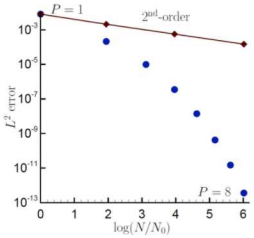

Spectral convergence

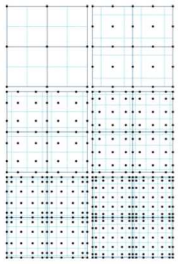

Dual-volume for promoted quad4

7

8 Incremental Approximate Pressure-Projection with Pressure Stabilization Errors

- Let the inverse of **A**, $\mathbf{A}^{-1}$ be approximated by $\mathbf{B}_2$ as a scalar, **τ (which is ~ time scale)**
- Let $\mathbf{B}_1$ be equal to the scaled Laplace operator, - **τL**

Momentum and Continuity: $\begin{bmatrix} A & 0 \\ D & -\tau L \end{bmatrix}\begin{bmatrix} \hat{u} \\ p^{n+1} \end{bmatrix} = \begin{bmatrix} \hat{f} \\ -D\tau G p^n \end{bmatrix}$ $\begin{matrix} A\hat{u} = f - Gp^n \\ D\hat{u} = \tau(Lp^{n+1} - DGp^n) \end{matrix}$

Nodal Projection: $\begin{bmatrix} I & \tau G \\ 0 & I \end{bmatrix}\begin{bmatrix} u^{n+1} \\ p^{n+1} \end{bmatrix} = \begin{bmatrix} \hat{u} \\ \hat{p} \end{bmatrix} + \begin{bmatrix} \tau G p^n \\ 0 \end{bmatrix}$ $\begin{matrix} u^{n+1} = \hat{u} - \tau G(p^{n+1} - p^n) \\ p^{n+1} = \hat{p} \end{matrix}$

- The new splitting and stabilization error is given by:

$$\begin{bmatrix} A & G \\ D & 0 \end{bmatrix}\begin{bmatrix} u^{n+1} \\ p^{n+1} \end{bmatrix} = \begin{bmatrix} f \\ 0 \end{bmatrix} + \begin{bmatrix} (I - A\tau)G(p^{n+1} - p^n) \\ \tau(L - DG)p^{n+1} \end{bmatrix}$$

Examples:
- Rhie-Chow (1983)
- Peric (1985)
- Fine-scale momentum residual, PSPG

- The above can be shown to hold a second-order temporal error (coming)
- Here, due to equal-order interpolation, i.e., collocation of primitives, **L** != **DG**
- Therefore, **L-DG** ~ 4th-order pressure stabilization (pressure oscillations damped)
- Therefore, pressure-stabilization error remains

8

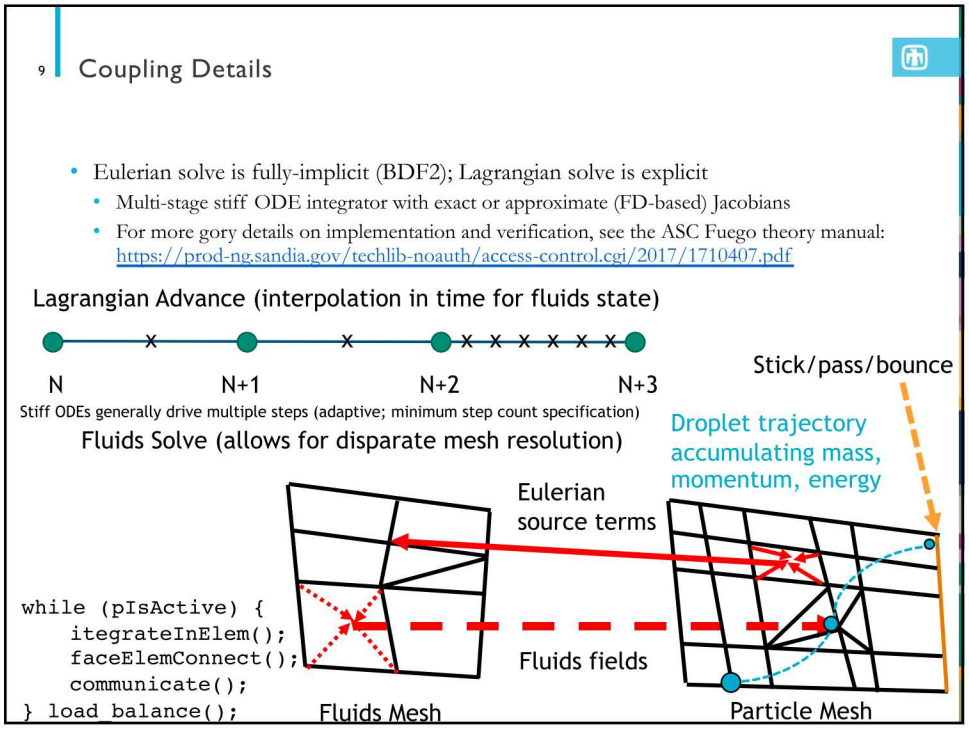
9
Coupling Details
• Eulerian solve is fully-implicit (BDF2); Lagrangian solve is explicit
• Multi-stage stiff ODE integrator with exact or approximate (FD-based) Jacobians
• For more gory details on implementation and verification, see the ASC Fuego theory manual:
https://prod-ng.sandia.gov/techlib-noauth/access-control.cgi/2017/1710407.pdf
Lagrangian Advance (interpolation in time for fluids state)
N
N+1
N+2
N+3
Stiff ODEs generally drive multiple steps (adaptive; minimum step count specification)
Fluids Solve (allows for disparate mesh resolution)
Stick/pass/bounce
Droplet trajectory accumulating mass, momentum, energy
Eulerian source terms
Fluids fields
while (pIsActive) {
itegrateInElem();
faceElemConnect();
communicate();
} load_balance();
Fluids Mesh
Particle Mesh

9

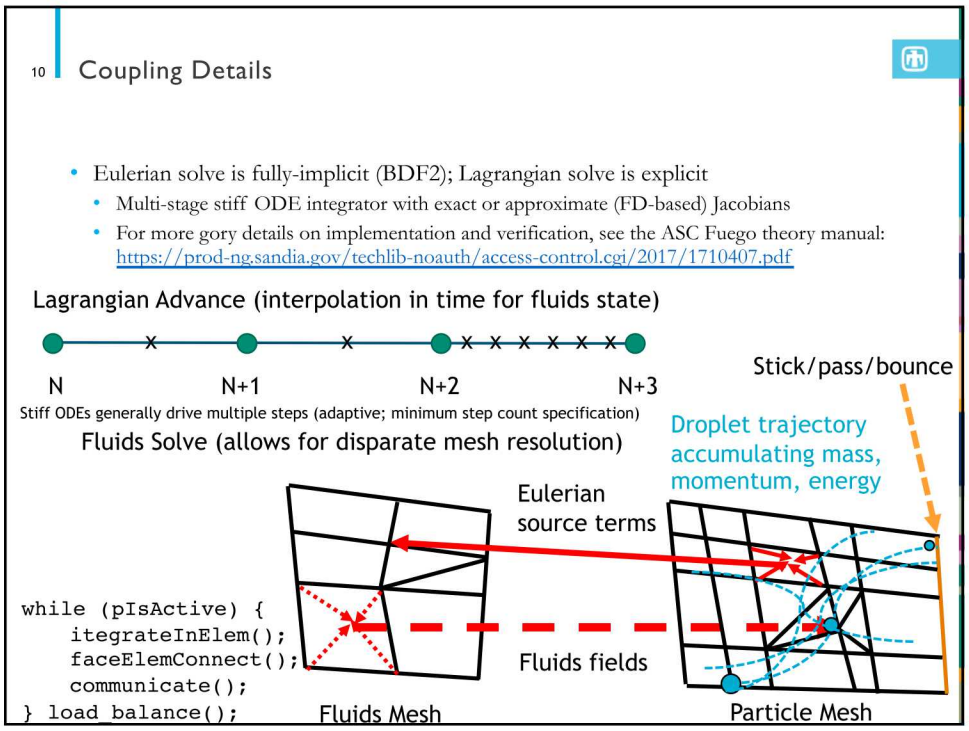
10
Coupling Details
• Eulerian solve is fully-implicit (BDF2); Lagrangian solve is explicit
• Multi-stage stiff ODE integrator with exact or approximate (FD-based) Jacobians
• For more gory details on implementation and verification, see the ASC Fuego theory manual:
https://prod-ng.sandia.gov/techlib-noauth/access-control.cgi/2017/1710407.pdf
Lagrangian Advance (interpolation in time for fluids state)
N
N+1
N+2
N+3
Stiff ODEs generally drive multiple steps (adaptive; minimum step count specification)
Fluids Solve (allows for disparate mesh resolution)
Stick/pass/bounce
Droplet trajectory accumulating mass, momentum, energy
Eulerian source terms
Fluids fields
while (pIsActive) {
itegrateInElem();
faceElemConnect();
communicate();
} load_balance();
Fluids Mesh
Particle Mesh

10

11 Confidence Established for Atypical Element Topos

Validation

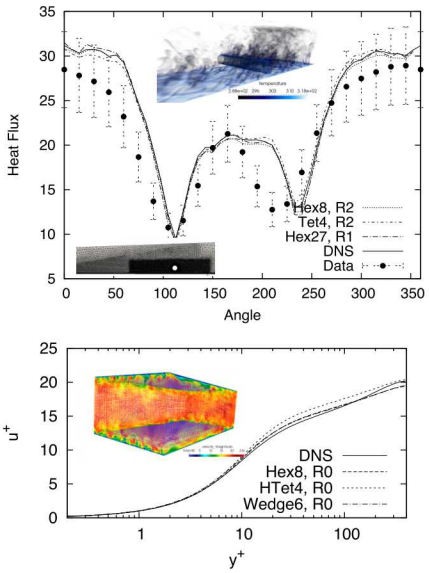

Verification

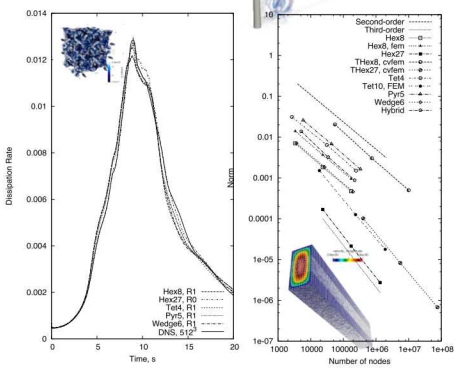

11

12 Confidence Established for Atypical Element Topos

Validation

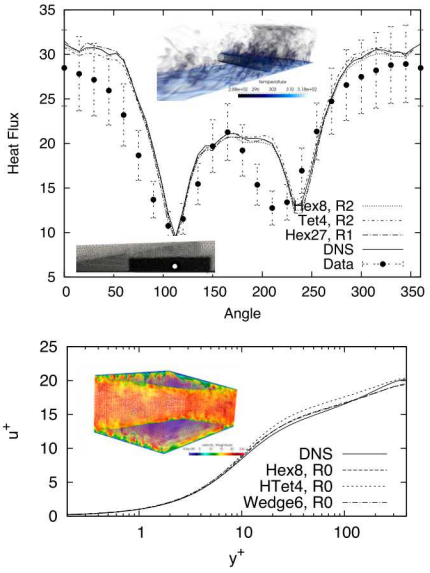

Verification

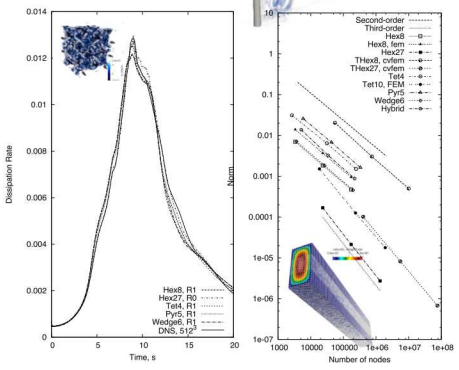

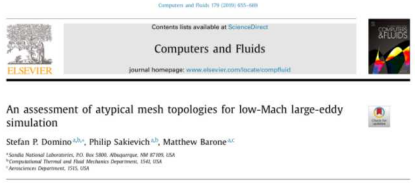
Contents lists available at ScienceDirect
Computers and Fluids
journal homepage: www.elsevier.com/locate/compfluid
An assessment of atypical mesh topologies for low-Mach large-eddy simulation
Stefan P. Domino, Philip Sakievich, Matthew Barone

12

13 A Note on High Performance Computing

- SNL is committed to High Performance Computing (HPC) to support is science and engineering objectives

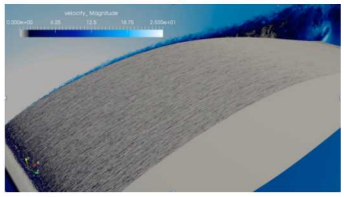

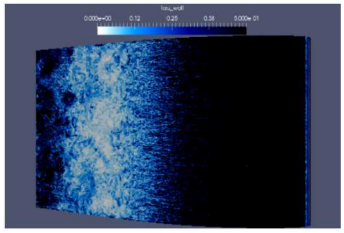

O(6) billion wind energy application

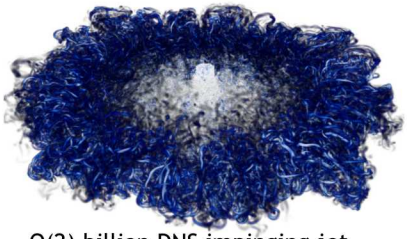

O(2) billion DNS impinging jet

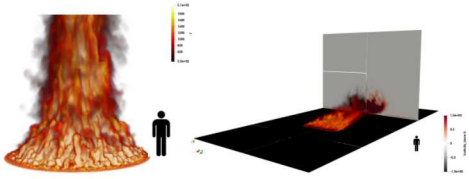

O(200) million multi-physics fire

13

14 Established Code Credibility; Evaporation Model Validation

- Ranz and Marshall, 1952 evaporation curves; 0% RH; See Fuego manual for verification

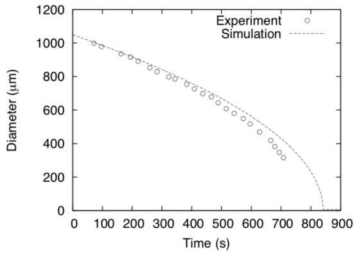

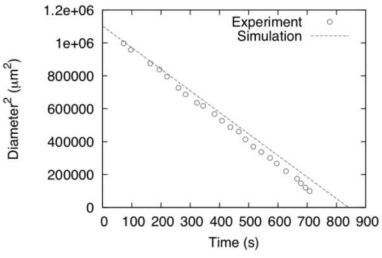

Validation
D^2 established

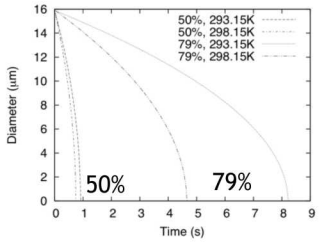

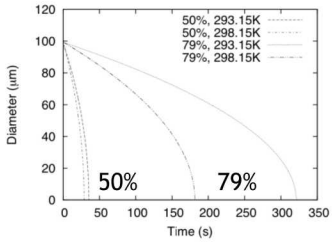

Exploration,
d = f(RH, T^a)
Miami vs ABQ

14

15 Quiescent Modeling Assumptions: *To Include or Not Include*: Evaporation and Coupling to Flow Field

- Large droplets (> 100 μm), regardless of modeling assumptions, deposit quickly
  - High crosswind velocity (10 m/s and higher) can increase deposition distance
- Small droplet nuclei (low-Stokes number) are highly coupled to fluid flow

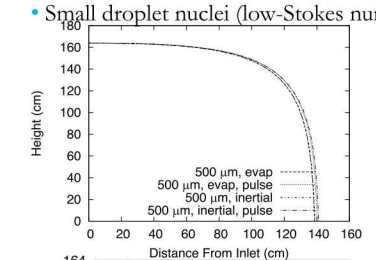

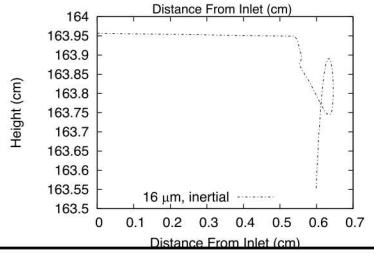

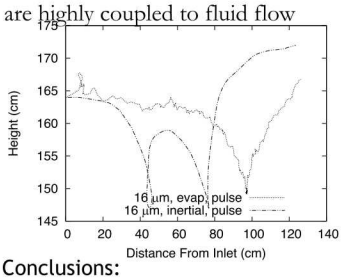

Conclusions:
- For O(1) scoping simulations, evaporation can probably be neglected
- Droplet transport should always be coupled to carrier fluid (cough, sneeze, breathing); Eulerian source terms (generally) << small
- Two-way coupling/droplet tracking is safest, especially since due to low numbers, the cost for droplet tracking is very [very] low

15

16 Established Code Credibility; Turbulent Fluid Mechanics

- L. Fan, Turbulent buoyant jets into stratified or flowing ambient fluids, Ph.D. thesis, California Institute of Technology (1967)
- LES is viable ***when you can resolve the flow*** as models are generally simplistic

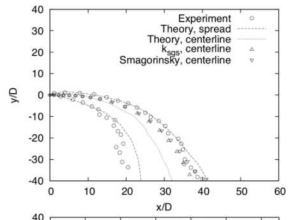

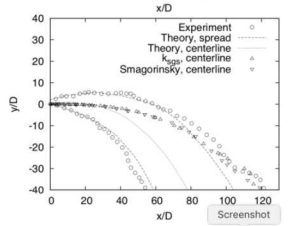

Fr 10 (~breathing)

Fr 40; uniform or stratified

Fr 40 (~coughing)

- Barolclinic terms small; Nicolette, Tieszen, Black, and Domino, SAND-20056273
- Buoyant instabilities low; Kyle and Sreenivasan, JCP 1993

16

17 Improved VVUQ: Automatic Structural Uncertainty

- Most LES validation studies establish structural uncertainty via direct model implementation and forward-calculations
- Is there a more efficient approach? Yes! Eigenvalue perturbation of the SGS stress (extension of RANS-based approach: Emory et al., *Phys. Fluids*, 2017)

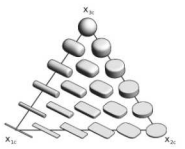

Barycentric triangle (see Lumley and Newman, *J. Fluid Mech.*, 1977)

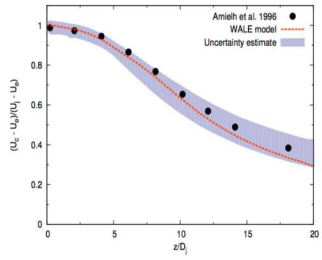

$$\tau_{ij}^{sgs} - \frac{\tau_{kk}^{sgs}}{3}\delta_{ij} = -2\nu_{sgs}\bar{S}_{ij},$$

$$a_{ij}^{res} = \frac{1}{\overline{u_k u_k}}\left(\overline{u_i u_j} - \frac{\overline{u_k u_k}}{3}\delta_{ij}\right) = v_{in}^{res}\Lambda_{nl}^{res}v_{jl}^{res}$$

$$a_{ij}^{sgs} = \frac{1}{\overline{u_k u_k}}\left(\tau_{ij}^{sgs} - \frac{\tau_{kk}^{sgs}}{3}\delta_{ij}\right) = v_{in}^{sgs}\Lambda_{nl}^{sgs}v_{jl}^{sgs},$$

Open jet

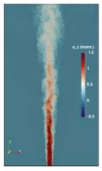

$$\overline{u_i u_j}^{*} = \bar{u}_i\bar{u}_j + \tau_{ij}^{sgs*} = \bar{u}_i\bar{u}_j + \overline{u_k u_k}^{*}a_{ij}^{sgs*} + \frac{\tau_{kk}^{sgs*}}{3}\delta_{ij},$$

with $\overline{u_k u_k}^{*} = \bar{u}_k\bar{u}_k + \tau_{kk}^{sgs*}$ and $a_{ij}^{sgs*} = v_{in}^{sgs*}\Lambda_{nl}^{sgs*}v_{jl}^{sgs*}.$

17

18 Improved VVUQ: Automatic Structural Uncertainty

- Most LES validation studies establish structural uncertainty via direct model implementation and forward-calculations
- Is there a more efficient approach? Yes! Eigenvalue perturbation of the SGS
  Flui

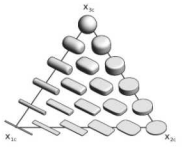

Barycentric triangle (see Lumley and Newman, *J. Fluid Mech.*, 1977)

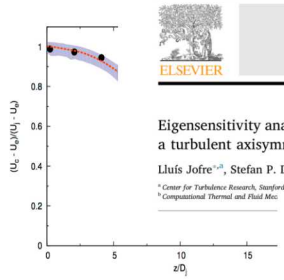

International Journal of Heat and Fluid Flow 77 (2019) 314–335

Contents lists available at ScienceDirect

International Journal of Heat and Fluid Flow

journal homepage: www.elsevier.com/locate/ijhff

Eigensensitivity analysis of subgrid-scale stresses in large-eddy simulation of a turbulent axisymmetric jet

Lluís Jofre[a,*], Stefan P. Domino[b], Gianluca Iaccarino[a]

[a] Center for Turbulence Research, Stanford University, Stanford, CA 94305, USA
[b] Computational Thermal and Fluid Mec

Flow Turbulence Combust (2018) 100:341–363
DOI 10.1007/s10494-017-9844-8

A Framework for Characterizing Structural Uncertainty in Large-Eddy Simulation Closures

Lluís Jofre[1] · Stefan P. Domino[2] · Gianluca Iaccarino[1]

$$^{res}_{nl}v^{res}_{jl}$$

$$)^{sgs}_{jl},$$

$$+\frac{\tau_{kk}^{sgs*}}{3}\delta_{ij},$$

$$^{*}\Lambda_{nl}^{sgs*}v_{jl}^{sgs*}.$$

Open jet

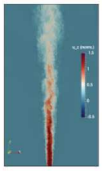

18

19 Simulation Tool Allows For Exploration of Droplet Transport in Quiescent and Crossflow Configurations

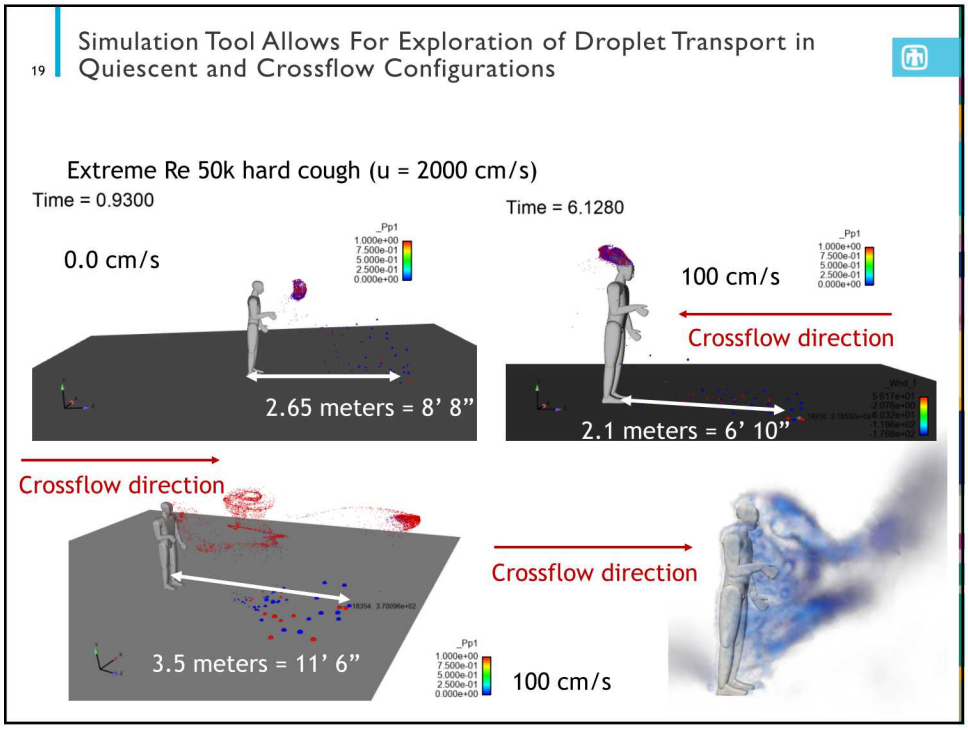

19

20 Outdoor Configurations, San Francisco, CA

- 10 foot circles; 8 foot separation only effective for droplets in quiescent conditions

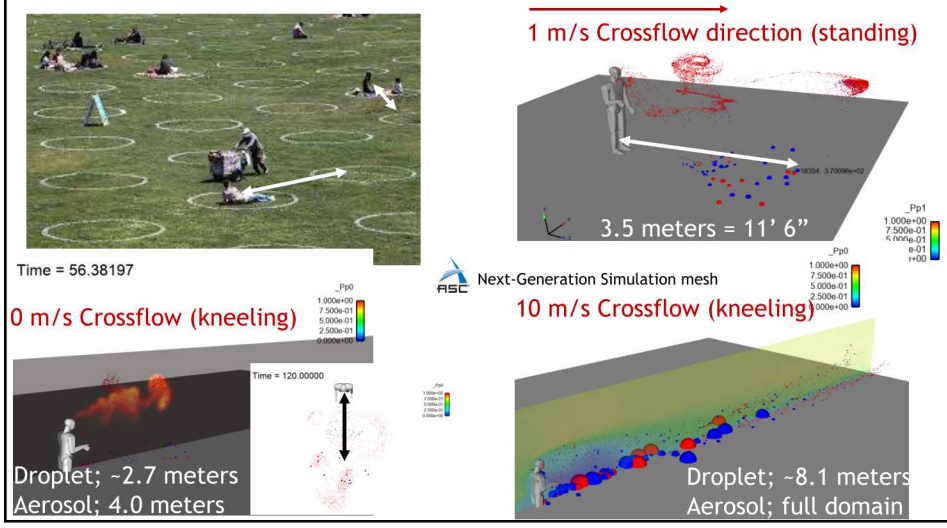

20

21 Investment in a Validation Dataset is Suggested

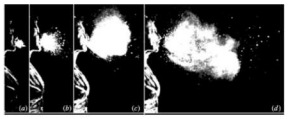

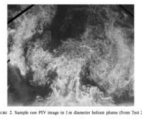

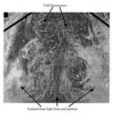

Current experiments are macroscopic (vs.... PIV, PLIF) O'Hern et al., JFM, 2005 Tieszen et al., C&F 2002

Lack of good finite-pulsed jet data

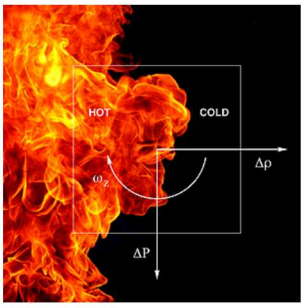

Thankfully, this application does not note substantial turbulent kinetic energy production via a baroclinic mechanism (smal density ratio, At# ~0.0

21

22 Conclusions

- Model Suite includes coupling between Eulerian and Lagrangian regions
- Mass, momentum, energy, species multi-phase turbulent flow
- Verification and Validation pedigree established for numerics/models
- Credibility established for evaporating physics and buoyant jets
- High-performance computing is a routine requirement

22

23 Extra

- Full talk includes more details

23

24 Pathogen Transport and Infection Mechanisms

- *Direct* and *Indirect* transmission mechanism

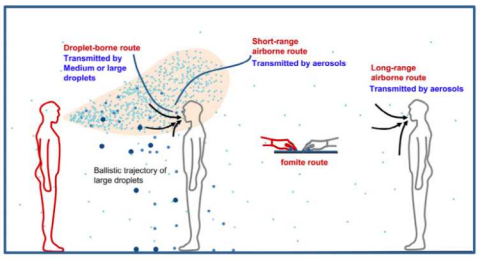

Wei and Li, A. J. Infec. Cont., 2016

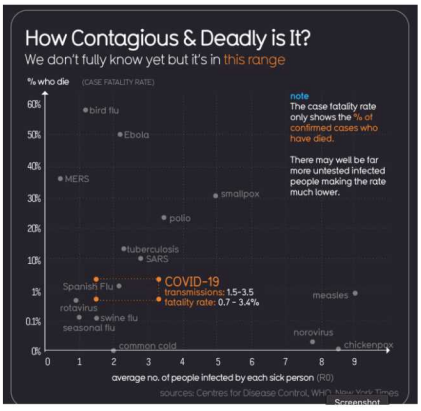

Informationisbeautiful.net

- ***Caveat***: currently, the open news cycle is not distinguishing between fluid mechanics transport of droplets emanating from a cough/sneeze and the likelihood of infection by either direct or indirect transmission
- As fluid mechanists, we can provide leadership towards answering the former while partnering with those who can speak towards pathogen viability and infection mechanism by providing detailed time-history trajectories

24

25 Viability of SARS-CoV-2 Aerosols

- Morris et al, "Aerosol and Surface Stability of SARS-CoV-2 as Compared with SARS-CoV-1", New England Journal of Medicine, April 16, 2020.

The half-lives of SARS-CoV-2 and SARS-CoV-1 were similar in aerosols, with median estimates of approximately 1.1 to 1.2 hours and 95% credible intervals of 0.64 to 2.64 for SARS-CoV-2 and 0.78 to 2.43 for SARS-CoV-1

We found that the stability of SARS-CoV-2 was similar to that of SARS-CoV-1 under the experimental circumstances tested. This indicates that differences in the epidemiologic characteristics of these viruses probably arise from other factors, including high viral loads in the upper respiratory tract and the potential for persons infected with SARS-CoV-2 to shed and transmit the virus while asymptomatic.[3,4]

Our results indicate that aerosol and fomite transmission of SARS-CoV-2 is plausible, since the virus can remain viable and infectious in aerosols for hours and on surfaces up to days (depending on the inoculum shed). These findings echo those with SARS-CoV-1, in which these forms of transmission were associated with nosocomial spread and super-spreading events,[5] and they provide information for pandemic mitigation efforts.

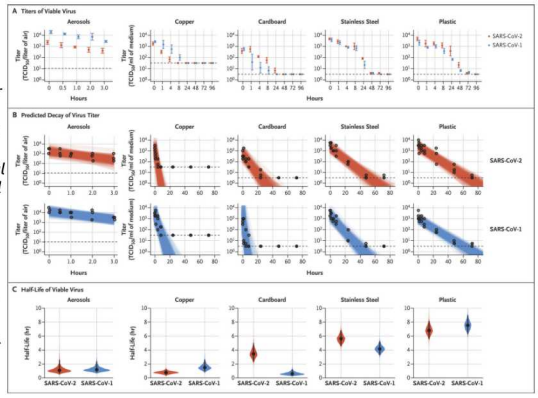

Excerpt from Morris et al., 2020

25

26 Modeling droplet dispersion from human coughs and sneezes in complex environments

- Objective: Deploy multi-physics mod/sim capability to understand droplet deposition and pathogen transport originating from human coughs to understand airborne transmission and surface contamination of COVID-19 in common public spaces

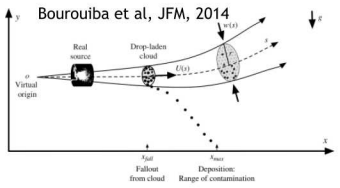

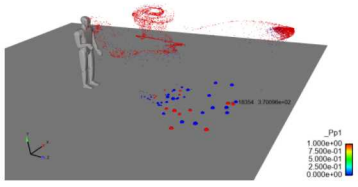

Fuego synthetic cough simulation with droplet distribution from Yang et al, J. Aersol Med, 2007 including pathogen probability

- Coughs are turbulent buoyant, multiphase plumes (Re~25K for coughs)
- Large droplets deposit while small droplets persist
- Evaporation rates, which are environment-specific, provides understanding towards what droplets deposit and those that persists
- Droplet nuclei can persist in the environment and *may* pose a long term risk to occupants

26

27 Why Sandia?

- Thermal/Fluids Core Competency rests in turbulent, buoyant, multi-phase transport

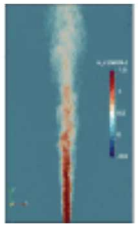

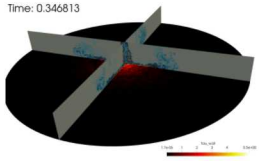

Turbulent jets

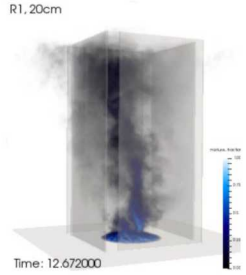

- Jofre, Domino, and Iaccarino, IJHT, 2019
- Domino, Sakiavich, Barone, Comp&F 2019
- Domino, JCP 2018

Buoyant plumes/whirls

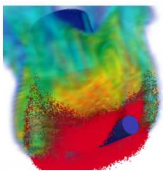

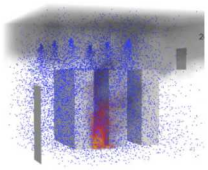

Deposition and suppression

Vortex dynamics

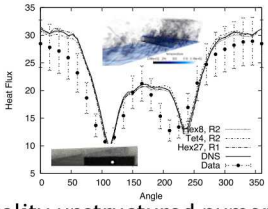

Quality unstructured numerics

27

28 Primary Objective: Establish a Credible High-Fidelity Multi-physics Tool

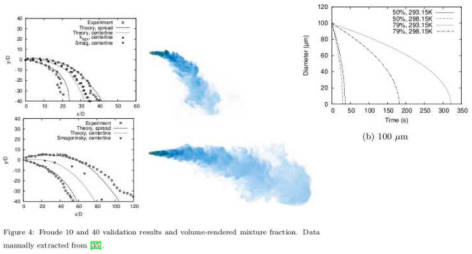

Figure 4: Froude 10 and 40 validation results and volume-rendered mixture fraction. Data manually extracted from [20].

Validation for droplet evaporation[Ranz&Marshall, 1952; Hamey, 1982] and plume dynamics[Fan, 1967]

- Goal: Close the credibility gaps from previous COVID-19 work

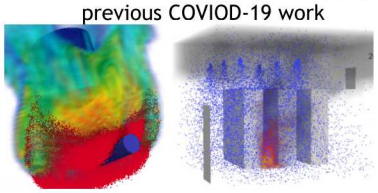

Deploy multi-physics code capability: Sierra/Fuego low-Mach turbulent reacting flow code with point-Lagrangian coupling

Time = 0.0600

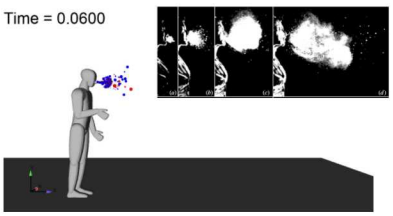

Time = 0.2000

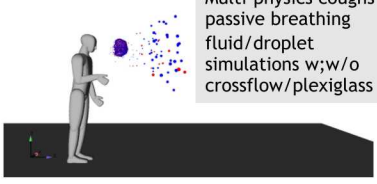

Multi-physics coughs passive breathing fluid/droplet simulations w;w/o crossflow/plexiglass

Time = 0.3400

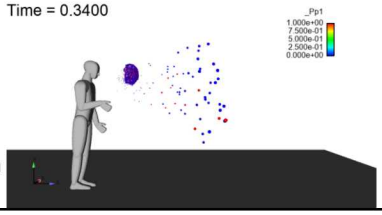

28

29 Droplet Size Distribution; Settling Speed; Physics Description

- Size, number and cough velocity are well characterized starting from as early as 1946
- Uncertainty in the literature

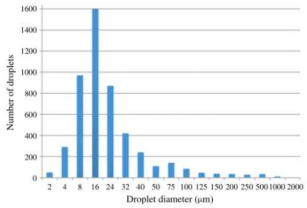

FIGURE 17. (Colour online) Histogram of droplet size in coughs (reproduced from Duguid 1946).

- Settling Speed:

$$m_p \frac{du_p}{dt} = \frac{m_p (u_p - u_f)}{\tau_p} + (m_p - m_f)g$$

$$u_p = \frac{d_p^2 (\rho_p - \rho_f)g}{18\mu_p}$$

Figures/Images again provided by Bourouiba et al, JFM, 2014

- Buoyancy, which affects plume dynamics, are known to be significant factors

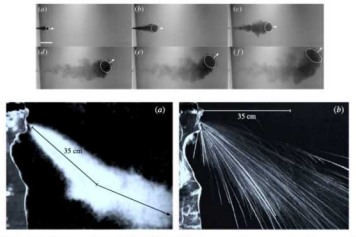

FIGURE 5. (Colour online) (a) The effect of buoyancy on the sneeze cloud is apparent in its upward curvature. (b) The large droplet trajectories are shown in the streak image recorded at 2000 f.p.s.

Modest room ventilation can easily suspend a droplet nuclei

Droplet Size (μm)	Settling Velocity (cm/s)	Settling Time for 2m height (s)	Evaporation Time (s)
100	~30	~6.6	~7
1	~3e-3	~66e3 (18.5 hr)	~7e-4

29

30 Findings: a) Droplet Nuclei Clustering/Persistence, b) Protective Shrouds are Effective for Primary Deposition Mitigation

Top wall not shown

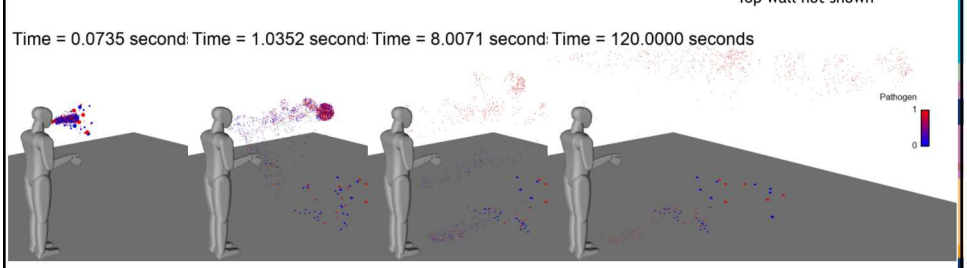

Pulsed nominal cough jet with (Top) and without (Bottom) protective shroud; R2 mesh

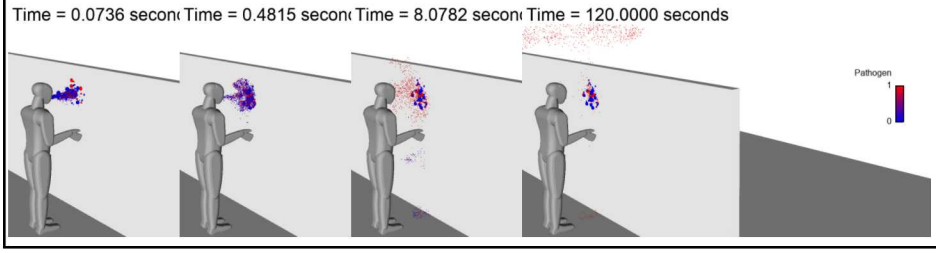

30

31 Findings: a) Droplet Nuclei Clustering/Persistence, b) Protective Shrouds are Effective for Primary Deposition Mitigation

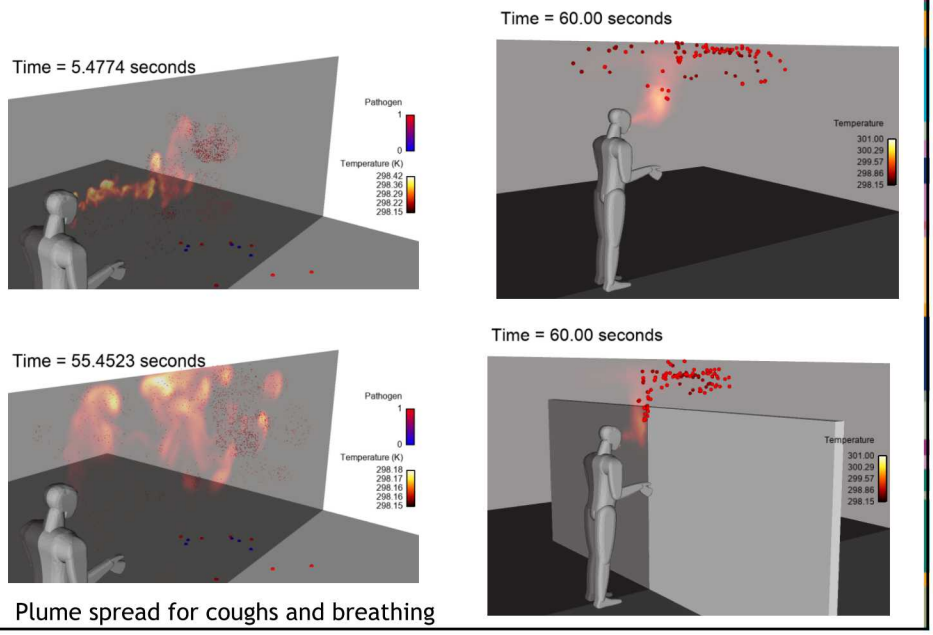

Plume spread for coughs and breathing

31

32 Findings: a) Droplet Nuclei Clustering/Persistence, b) Protective Shrouds are Effective for Primary Deposition

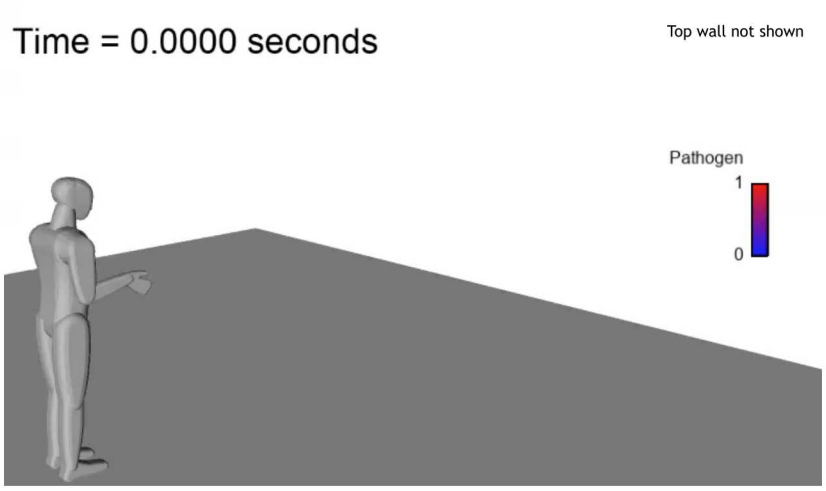

Re 25,000

- Classic axisymmetric jet shedding drives droplet clustering
- Primary droplet cloud in addition to secondary buoyant plumes

32

33 Findings: a) Droplet Nuclei Clustering/Persistence, 2) Protective Shrouds are Effective for Primary Deposition

Top wall not shown

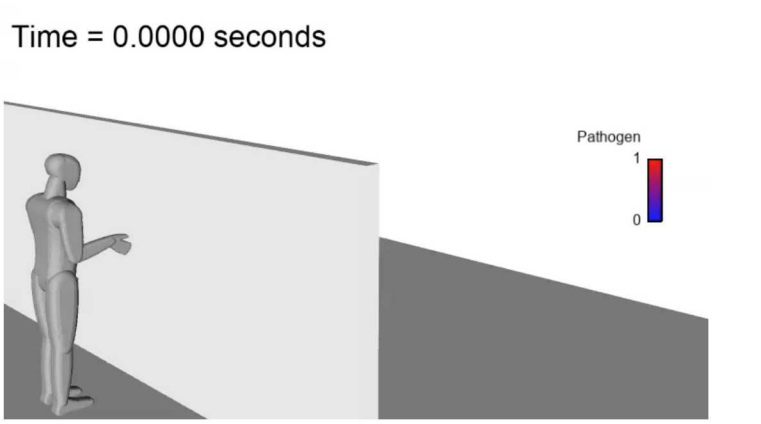

Re 25,000

- High- streamwise curvature impinging jet drives ring impingement clustering
- Persistence of droplet nuclei is noted

33

34 Buyer-beware: low-Resolution Simulations Underpredict Vortex Shedding from Primary Jet

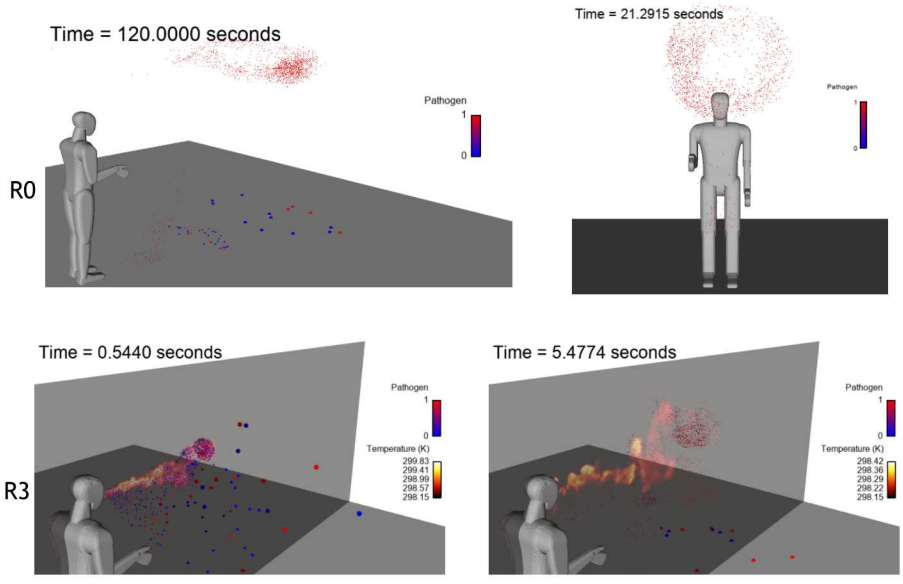

R3 ~ O(250) million elements

34

35 The Role of Protective Shrouds; Passive Breathing in Zero crossflow

Wan et. al, Particle Size Concentration Distribution and Influences on Exhaled Breath Particles in Mechanically Ventilated Patients; 2014

Droplets persist while forming a concentrated cloud at the protective shroud

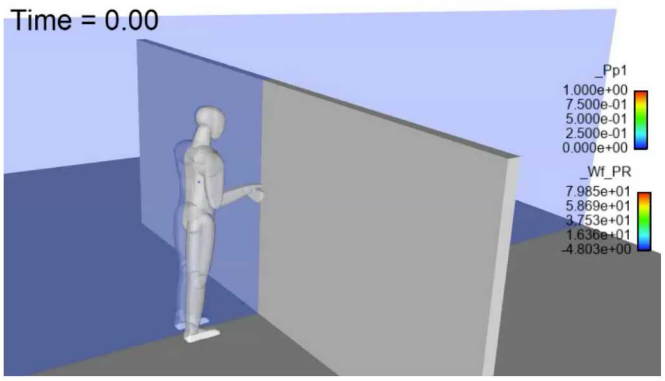

- 1, 2, and 3 micron spray distribution; 120e-12 g injection over 4 seconds; sinusoidal breath of 100 cm/s
- Low velocity and small droplets render direct transmission unlikely, however, as with previous simulations, droplet nuclei persist - now at low concentrations

35

36 The Role of Protective Shrouds; Passive Breathing in Zero crossflow

Wan et. al, Particle Size Concentration Distribution and Influences on Exhaled Breath Particles in Mechanically Ventilated Patients; 2014

Droplets persist while forming a cloud approximately 1.5 meters from source

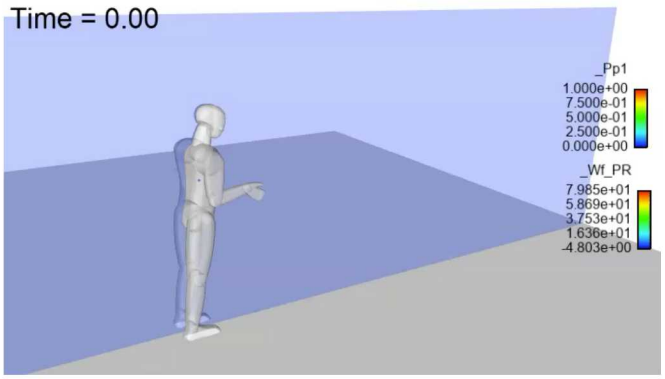

- 1, 2, and 3 micron spray distribution; 120e-12 g injection over 4 seconds; sinusoidal breath of 100 cm/s
- Low velocity and small droplets render direct transmission unlikely, however, as with previous simulations, droplet nuclei persist - now at low concentrations

36

37 Crossflow Animations

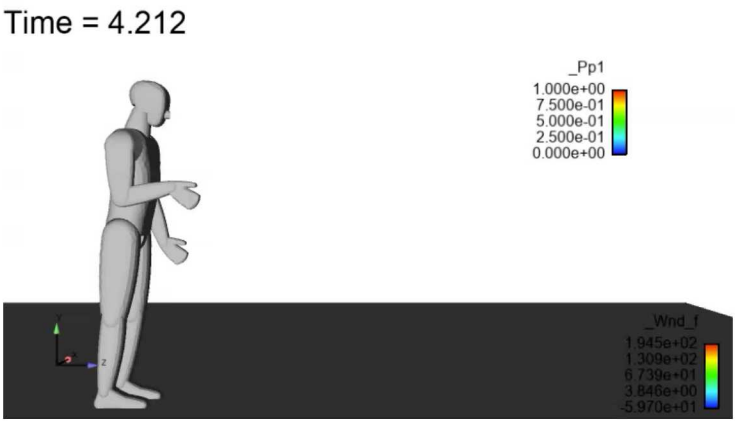

_Pp1 = pathogen

Crossflow direction

1 m/s crossflow (back)

Log-normal droplet distribution fit matching mass

37